Differences in Particle Deposition Between Members of Imaging-Based Asthma Clusters

Jiwoong Choi, PhD,[1,2] Lawrence J. LeBlanc, MS,[1,2] Sanghun Choi, PhD,[3] Babak Haghighi, PhD,[1,2]
Eric A. Hoffman, PhD,[4] Patrick O'Shaughnessy, PhD,[5] Sally E. Wenzel, MD,[6] Mario Castro, MD,[7]
Sean Fain, PhD,[8,9] Nizar Jarjour, MD,[10] Mark L. Schiebler, MD,[9] Loren Denlinger, MD, PhD,[10]
Renishkumar Delvadia, PhD,[11] Ross Walenga, PhD,[11] Andrew Babiskin, PhD,[11] and Ching-Long Lin, PhD[1,2]

Abstract

Background: Four computed tomography (CT) imaging-based clusters have been identified in a study of the Severe Asthma Research Program (SARP) cohort and have been significantly correlated with clinical and demographic metrics (*J Allergy Clin Immunol* 2017; 140:690–700.e8). We used a computational fluid dynamics (CFD) model to investigate air flow and aerosol deposition within imaging archetypes representative of the four clusters.

Methods: CFD simulations for air flow and 1–8 μm particle transport were performed using CT-based airway models from two healthy subjects and eight asthma subjects. The subject selection criterion was based on the discriminant imaging-based flow-related variables of J(Total) (average local volume expansion in the total lung) and D_h^*(sLLL) (normalized airway hydraulic diameter in the left lower lobe), where reduced J(Total) and D_h^*(sLLL) indicate reduced regional ventilation and airway constriction, respectively. The analysis focused on the comparisons between all clusters with respect to healthy subjects, between cluster 2 and cluster 4 (nonsevere and severe asthma clusters with airway constriction) and between cluster 3 and cluster 4 (two severe asthma clusters characterized by normal and constricted airways, respectively).

Results: Nonsevere asthma cluster 2 and severe asthma cluster 4 subjects characterized by airway constriction had an increase in the deposition fraction (DF) in the left lower lobe. Constricted flows impinged on distal bifurcations resulting in large depositions. Although both cluster 3 (without constriction) and cluster 4 (with constriction) were severe asthma, they exhibited different particle deposition patterns with increasing particle size. The statistical analysis showed that D_h^*(sLLL) plays a more important role in particle deposition than J(Total), and regional flow fraction is correlated with DF among lobes for smaller particles.

Conclusions: We demonstrated particle deposition characteristics associated with cluster-specific imaging-based metrics such as airway constriction, which could pertain to the design of future drug delivery improvements.

Keywords: airway constriction, cluster analysis, computational fluid dynamics, inhaled corticosteroid, particle deposition, quantitative computed tomography

[1]Department of Mechanical Engineering and [2]IIHR-Hydroscience and Engineering, The University of Iowa, Iowa City, Iowa.
[3]School of Mechanical Engineering, Kyungpook National University, Daegu, Republic of Korea.
Departments [4]Radiology and [5]Occupational and Environmental Health, The University of Iowa, Iowa City, Iowa.
[6]Division of Pulmonary, Allergy, and Critical Care Medicine, University of Pittsburgh, Pittsburgh, Pennsylvania.
[7]Departments of Internal Medicine and Pediatrics, Washington University School of Medicine, St. Louis, Missouri.
Departments of [8]Medical Physics and [9]Radiology, School of Medicine and Public Health, University of Wisconsin, Madison, Wisconsin.
[10]Division of Pulmonary Medicine and Critical Care, Department of Medicine, School of Medicine and Public Health, University of Wisconsin, Madison, Wisconsin.
[11]Office of Research and Standards, Office of Generic Drugs, Center for Drug Evaluation and Research, U.S. Food and Drug Administration, Silver Spring, Maryland.

Introduction

AEROSOLIZED BRONCHODILATOR AND CORTICOSTEROID INHALATIONS are common treatments for asthma. Drug administration is most commonly performed through metered dose inhaler (MDI) or dry powder inhaler. Current delivery methods are limited by low deposition in the peripheral lung regions due to lung structure variability, device misuse, aerosol size limitations, and inconsistent inspiration patterns.[1]

Lung morphology and physiology characteristics vary considerably between patients and influence air and drug delivery, resulting in deposition variability.[2,3] Subject's age, weight, asthmatic severity, and other factors altogether dictate lung makeup and function.[4] Studying with a large sample size to achieve statistically relevant results for the global population is not practical due to complexity and cost of the study. Characterization of intersubject variability is critical for improved lung and drug studies.[5–8] The need for classifying subjects accurately into clusters characterized by distinct structural and functional features is a potentially important advancement for pulmonary drug delivery studies.[5,9,10]

Cluster analysis has shown a promise in evaluating the heterogeneity of asthma symptoms and characteristics. Subjects have been grouped based on common clinically measured phenotypes, patient history, and quality of life metrics.[10–13] Phenotypes included characteristics such as spirometry-derived variables and inflammatory blood and sputum cell counts. A recent study in an asthmatic population involved multiscale imaging-based cluster analysis (MICA) using structural and functional variables to establish clusters which correlated well with clinical phenotypes.[5] The MICA subdivided nonsevere and severe asthmatic subjects into four distinct clusters using local and global quantitative computed tomography (CT) variables.

Due to challenges associated with evaluating intercluster variability, *in silico* modeling has become a preferred method for this lung research. Numerical models used for inhaled particle delivery studies involve computational fluid dynamics (CFD) simulations, combined with experimental methods for validation.[14,15] When combined with imaging-based geometries, realistic geometries and flow ventilations can be recreated.[8,16–19] Computer models could predict detailed information and can evaluate deposition patterns at lung, lobar, or airway branch levels.[6,14,20]

The purpose of this study was to use the airway structural and parenchyma functional measurements of representative cluster patients to characterize four distinct *in silico* archetypes by exploring the CFD-derived estimates of particle deposition patterns in asthma subpopulations. The ultimate goal is to improve drug administration to asthmatics through cluster membership.

Materials and Methods

Subject selection for CFD

Lung CT images at total lung capacity (TLC) and functional residual capacity (FRC) were acquired from the University of Pittsburgh and University of Wisconsin, with approval from respective institutional review boards, as part of the Severe Asthma Research Program (SARP). Acquisi-

tion methods and imaging protocols could be found in the reference.[21]

Choi et al.[5] identified 10 most discriminant variables from 57 imaging-based structural and functional variables for clustering. The top four variables ranked by Wilk's λ value (Table 1) were the average Jacobian determinant in the whole lung [J(Total)], the air trapping score in the whole lung [AirT%(Total)], the normalized airway hydraulic diameter in the left lower lobe (LLL) subset [D_h*(sLLL)], and the average normalized airway wall thickness in the right upper lobe (RUL) subset [WT*(sRUL)]. Specifically, J is defined as the local lung volume ratio, v^{TLC}/v^{FRC}, where v^{TLC} and v^{FRC} denote a local lung volume at TLC and its corresponding volume at FRC, respectively, at the voxel level. D_h* is the hydraulic diameter normalized by the predicted diameter of the trachea.[21]

Among the four variables, air trapping (AirT%) and wall thickness (WT*) were less likely to have a direct impact on air flow and particle behavior. Therefore, J(Total) (a functional variable affecting flow distribution) and D_h*(sLLL) (a structural variable measuring airway constriction) were regarded as the most discriminant variables in characterizing air flow and particle deposition among clusters. Overall, cluster 1 had increased J(Total), whereas cluster 2 and cluster 4 had decreased J(Total) and D_h*(sLLL) as noted by arrows ↑ (increase) and ↓ (decrease) in Table 1. The differences were statistically significant ($p < 0.001$).[5]

We selected a total of 10 subjects to examine the effects of the above two variables on air flow and particle deposition, using three-dimensional (3D) CFD simulations. The first set of six subjects comprised one healthy female (HF), one healthy male (HM), and one subject from each of the four asthma clusters, denoted by HF, HM, C1, C2, C3, and C4, respectively, in Table 2. The selection criterion was subjects with increased J in cluster 1 and decreased J and D_h* in cluster 2 and cluster 4 in comparison with healthy subjects (see J(Total) and D_h*(sLLL) with arrows ↑ and ↓ in Tables 1 and 2).

To assess the effect of intracluster variability (namely, intersubject variability within clusters) on intercluster variability, we selected two additional subjects from each of cluster 3 and cluster 4. The reason for focusing on the two clusters is of clinical relevance and implication due to their treatment with inhaled corticosteroids (ICSs).[5] Namely, both were severe asthmatics, but only cluster 4 was characterized by airway constriction [D_h*(sLLL)↓] in association with persistently altered lung function [J(Total)↓], which might lead to different inhaled drug aerosol deposition than cluster 3.

The selection criterion for these additional subjects was based on the minimal deviation from the cluster-mean D_h*(sLLL) because airway narrowing in the sLLL was a key feature in differentiating the two clusters. The two additional cluster 3 (or 4) subjects were denoted by C3a and C3b (or C4a and C4b) in Table 2.

We then performed biserial correlation analysis to evaluate the association of the continuous variables of D_h*(sLLL) and J(Total) with the dichotomous variables of cluster number 3 and 4 between the three cluster 3 subjects (C3, C3a, and C3b) and the three cluster 4 subjects (C4, C4a, and C4b). The biserial correlation coefficients of D_h*(sLLL) and J(Total) with the two groups were −0.804 and −0.885, respectively, indicating that the two variables

TABLE 1. THE TOP FOUR IMAGING-BASED VARIABLES RANKED BY WILK'S λ VALUE

	Wilk's λ value	Cluster 1 (n=80)	Cluster 2 (n=59)	Cluster 3 (n=68)	Cluster 4 (n=41)	p	Healthy (n=61)
J(Total)	0.317	2.48 ($\uparrow$)	1.69 ($\downarrow$)	1.91	1.47 ($\downarrow$)	<0.001	2.05
AirT%(Total)	0.177	5.8	8.6	8.9	29.7	<0.001	7.8
D_h*(sLLL)	0.123	0.338	0.269 ($\downarrow$)	0.344	0.301 ($\downarrow$)	<0.001	0.338
WT*(sRUL)	0.098	0.609	0.587	0.646	0.607	<0.001	0.612

Arrows $\uparrow$ and $\downarrow$ in parentheses denote increase and decrease, respectively, of cluster-mean J(Total) and D_h*(sLLL) in comparison with healthy subjects with a significance level of $p < 0.001$.

AirT%, air trapping percentage; D_h*, normalized hydraulic diameter; J, Jacobian determinant; sLLL, left lower lobe subset; sRUL, right upper lobe subset; WT*, normalized wall thickness.

are highly differentiable between the two groups. The negative correlation means that the selected cluster 4 subjects had statistically smaller D_h*(sLLL) and J(Total) than the selected cluster 3 subjects.

Airway geometries

We constructed 3D airway geometries using CT images obtained at TLC for each subject using a commercial software (Apollo, VIDA Diagnostics, Coralville, IA) and in-house geometrical modeling methods.[18,22] The SARP imaging protocol did not include the imaging of the upper airways; thus, we used a laryngeal model[22] that creates a glottal constriction in the trachea to produce inspiratory turbulent laryngeal jet (see also Air Flow Simulation section and Particle Simulation section). Thus, the 3D airway geometry consisted of the glottal constriction, trachea, and intrathoracic central airways. Figure 1 shows an example of the CT-based airway skeleton and 3D geometry.

Based on the CT-resolved central airways, a one-dimensional (1D) airway tree extending to terminal bronchioles was generated using the volume filling technique.[23,24] The diameters of the branches beyond CT resolution were determined by the lobar average of parent-to-child diameter ratio, and a random heterogeneity was applied to model asthmatic constriction based on the lobar D_h*.[25]

Air flow simulation

Subject-specific flow rates were prescribed at the supraglottal inlet. The inhalation flow rate was determined by Equations (1) and (2), mimicking slow and deep breathing activated by an MDI at the start of inhalation.[6] Inhaled air volume was set to inspiratory capacity (IC), calculated from TLC and FRC images. For all cases, the time to peak inspiration (T_{PI}) was set to 1.25 seconds. The maximum volumetric flow rate (Q_{PI}) at peak inspiration (PI) was calculated in Equation (1) with IC, T_{PI}, and an inhalation period of $T = 5.0$ seconds for all cases.[6]

$$Q_{PI} = \frac{2\pi\, IC}{\pi T_{PI} + 4(T - T_{PI})}. \tag{1}$$

$$Q(t) = \frac{Q_{PI}}{T_{PI}} t; \quad 0 \le t \le T_{PI}. \tag{2}$$

Flow conditions at PI together with the tracheal Reynolds numbers ($Re_{trachea}$) based on Q_{PI} and the tracheal diameter are reported in Table 2.

Because the values of $Re_{trachea}$ for all cases were greater than the critical Re of about 2000 for turbulent pipe flow, we used a synthetic eddy method (SEM) at the supraglottal

TABLE 2. OVERVIEW OF DEMOGRAPHICS, IMAGING-BASED FEATURES, AND COMPUTATIONAL FLUID DYNAMICS FLOW INLET CONDITIONS AT PEAK INSPIRATION OF THE SELECTED SUBJECTS

	HF	HM	C1	C2	C3	C3a	C3b	C4	C4a	C4b
Demography										
Sex	Female	Male	Female	Male	Female	Female	Female	Male	Male	Male
Age (years)	29	28	20	52	49	38	23	51	58	51
Weight (kg)	61.5	99	58.6	111.8	85.1	106.8	72.3	103	116.3	88.5
Asthma severity	N/A	N/A	Nonsevere	Nonsevere	Severe	Severe	Severe	Severe	Severe	Severe
Key imaging-based features of the selected subjects										
J(Total)	2.0	2.4	3.3 ($\uparrow$)	1.8 ($\downarrow$)	1.9	2.2	2.2	1.4 ($\downarrow$)	1.7 ($\downarrow$)	1.7 ($\downarrow$)
D_h* (sLLL)	0.35	0.38	0.37	0.24 ($\downarrow$)	0.43	0.34	0.35	0.23 ($\downarrow$)	0.30 ($\downarrow$)	0.30 ($\downarrow$)
CFD flow inlet conditions at PI										
IC (L)	2.5	3.4	3.0	2.5	2.7	2.4	3.2	1.8	2.9	2.5
Q_{PI} (L/min)	50.2	66.7	60.2	50.5	53.3	48.5	63.4	35.8	57.1	50.5
D_h* (trachea)	1.17	0.99	0.88	0.94	1.23	1.07	1.11	0.97	0.85	1
$Re_{trachea}$	4364	5364	6647	3905	3894	4047	5323	2742	4881	3715

Sex was considered when selecting subjects to eliminate sex bias. Arrows $\uparrow$ and $\downarrow$ in parentheses denote increase and decrease, respectively, of cluster-mean J(Total) and D_h*(sLLL) in comparison with healthy subjects with a significance level of $p < 0.001$.

CFD, computational fluid dynamics; D_h*, normalized hydraulic diameter; HF, healthy female; IC, inspiratory capacity; J, Jacobian determinant; PI, peak inspiration; Q_{PI}, maximum volumetric flow rate at peak inspiration; Re, Reynolds number.
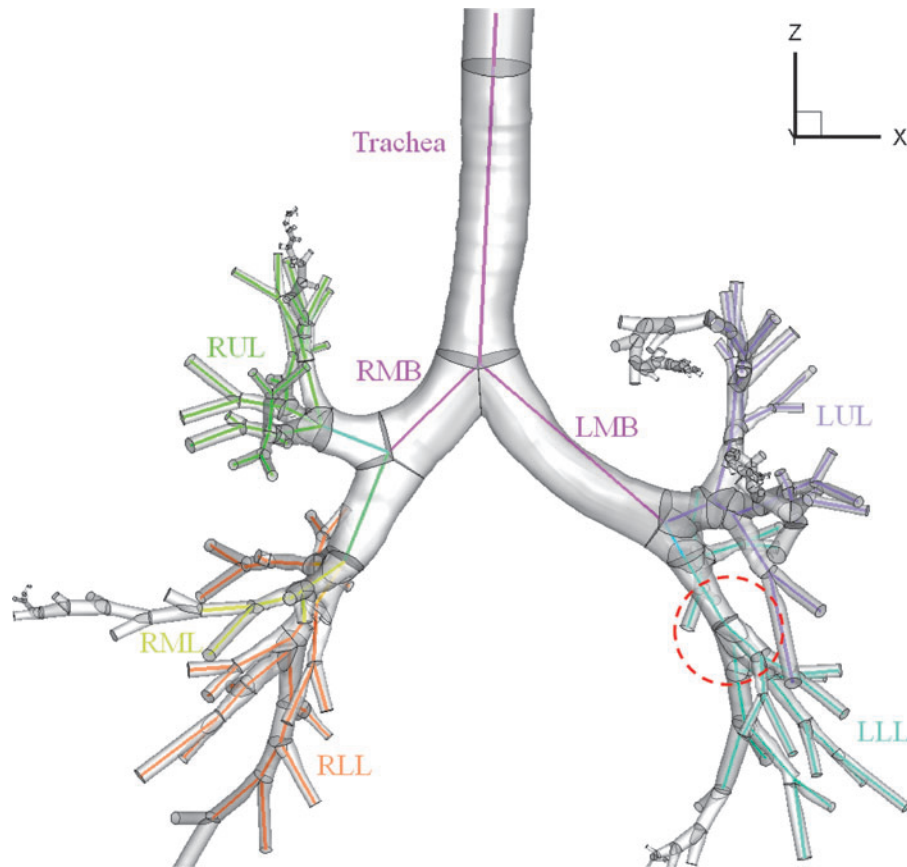
FIG. 1. CT-based 3D–1D geometry of HM subject with the five lobes and major branches labeled. The colored lines distinguish the five lobes and represent the 1D skeleton that maps out the airway branching patterns and provides branching angles, lengths, and average diameters for 3D geometry construction. The region highlighted by a red circle references the lung location of Figure 4. 1D, one-dimensional; 3D, three-dimensional; CT, computed tomography; HM, healthy male; LMB, left main bronchus; LLL, left lower lobe; LUL, left upper lobe; RLL, right lower lobe; RMB, right main bronchus; RML, right middle lobe; RUL, right upper lobe.

entrance in the larynx[26] to generate turbulent flow inlet conditions. To construct physiologically consistent flow rate distributions, we first estimated local static air-volume change based on image registration between CT images at TLC and FRC.[27,28] We then used it as an initial condition for a 1D flow model that solves 1D continuity and energy equations in a successive branching structure to account for pressure drop due to unsteadiness, kinetic energy, and viscous dissipation.[29] A static compliance model was used to estimate pressure at acinar region with the assumption of uniform pressure at pleural region.[25,30]

The predicted flow rate distributions were then imposed at terminal bronchioles for 3D CFD simulations and were used to calculate mass flow fractions among the five lobes (QF). Because turbulent flow might affect interlobe particle distribution,[26] we used an in-house large eddy simulation (LES) technique[8,31–35] to resolve energy-containing turbulent eddy structures. Thus, the effect of turbulent dispersion on particle transport was accounted for in the calculation of particle trajectories. The biserial correlation analysis of IC, Q_{PI}, D_h^*(trachea), and $Re_{trachea}$ between the selected cluster 3 and cluster 4 subjects yielded the respective correlation coefficients of −0.419, −0.428, −0.829,

and −0.386. The small coefficient for $Re_{trachea}$ suggested that turbulent flow may contribute insignificantly to particle deposition patterns between the two clusters.

Mesh sizes were determined such that the average distance from the boundary wall covered by the first element was less than 9 wall units ($y^+ < 9$) at PI.[8] The number of tetrahedral elements ranged from about 8 to 14 million, depending on subject-specific flow conditions.

Particle simulation

Lagrangian particle tracking simulations followed particles on an individual basis through the flow field. This method has been previously verified with *in vivo* data.[17,26] With this method the particle deposition efficiencies predicted using the flow field simulated by the laryngeal model agreed well with those predicted by the airway model with the upper airways.[22] Brownian motion was not considered, and simulations were performed with mass median aerodynamic diameters (MMAD) of 1, 2, 4, and 8 μm, which span the range of aerosolized drug delivery.[20]

At the start of the inspiration simulation, 200,000 spherical particles were released uniformly at the laryngeal inlet.
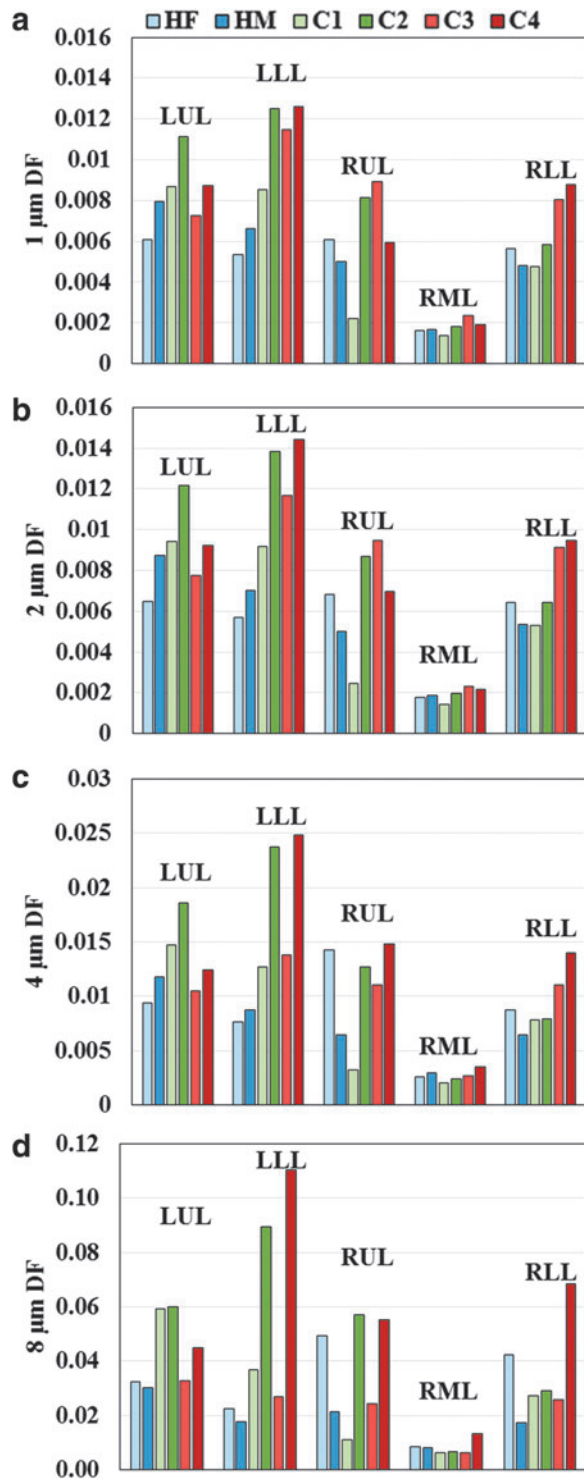
FIG. 2. Regional DF for (a) 1, (b) 2, (c) 4, and (d) 8 μm diameter particles. Plots are separated by lobe and cluster. DF for all five lobes between clusters was significantly different ($p < 0.05$). DF, deposition fraction; HF, healthy female; HM, healthy male; LLL, left lower lobe; LUL, left upper lobe; RLL, right lower lobe; RML, right middle lobe; RUL, right upper lobe.

Particle deposition was quantified with deposition fraction (DF) and deposition density (DD) for CT resolved branches. DF is the deposited particles in a region normalized to the total particles in the simulation (N_p). DD denotes the

number of deposited particles per unit surface area (SA) of a region. In Equations (3) and (4), $N_{p,ent.}$ and $N_{p,exit}$ represent number of particles entering and exiting a region, respectively, and their difference is the number of deposited particles in a region.

$$DF = \frac{N_{p,ent.} - N_{p,exit}}{N_p}. \tag{3}$$

$$DD = \frac{N_{p,ent.} - N_{p,exit}}{SA}. \tag{4}$$

Note that deposition efficiency (not discussed here) is defined as $(N_{p,ent.} - N_{p,exit})/N_{p,ent.}$.

Statistical analysis of deposition results

For statistical analysis, we used two-way analysis of variance (two-way ANOVA) with Tukey's *post hoc* test (R software version 3.1.1) for comparisons of DF on generational, lobar, and whole lung levels. Airways were grouped by lobe and by generation numbers 0–2, 3–4, 5–6, and 7–8, and depositions in each lobe and deposition in each branch of the appropriate generation range were used to evaluate significance, respectively. All *p*-values are two sided, with Bonferroni-corrected pairwise comparisons between individual groups. A $p < 0.05$ was considered to indicate statistical significance in all tests.

Biserial correlation analysis was performed to calculate the correlations between imaging-based variables and cluster numbers (namely, between continuous and dichotomous variables for cluster 3 and cluster 4 only), and unpaired Wilcoxon test was performed to compare continuous variables between the three cluster 3 and three cluster 4 subjects.

Results

This section compares cluster differences in terms of particle DFs and DDs with respect to characteristic alterations of each cluster. Cluster 1 subjects are nonsevere in majority and have functional and structural characteristics relatively similar to healthy subjects.[5] Two-way ANOVA with *post hoc* tests of lobar and generational DFs found no significant differences between HM and HF and between C1 and C2 ($p > 0.05$). Due to dissimilarities to the other asthmatic clusters, the following deposition results focus on the subjects in clusters 2, 3, and 4.

Particle DF

Lobar DFs for the first set of six subjects were plotted in Figure 2 to assess intercluster variability. DFs in the five lobes between clusters were found to be significantly different ($p < 0.05$) by two-way ANOVA and *post hoc* test. For large particle diameters (4 and 8 μm), C2 and C4 had greater DF values compared to other subjects, and the DF differences between subjects with normal versus constricted airways (D_h^*) increased with particle diameter. Specifically, with increasing particle size, DF increased more rapidly in the LLL than other lobes for C2 and C4, while DF only slightly increased for C3.
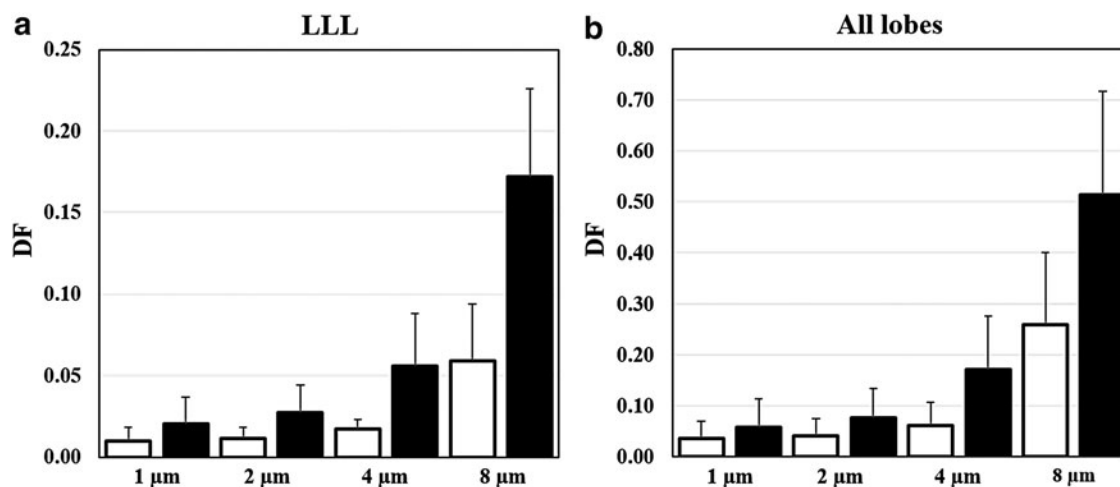
FIG. 3. Mean deposition fractions of 1, 2, 4, and 8 μm particles in (a) LLL and (b) all the lobes for the three C3 (blank) and C4 (filled) subjects, respectively. Error bars indicate standard deviations.

To assess the effect of intracluster variability on intercluster variability, Figure 3 compared DFs in the LLL of the three cluster 3 and the three cluster 4 subjects. The cluster 4 subjects with airway constriction had consistently higher DFs than the cluster 3 subjects in the LLL (Fig. 3a) and all the lobes (Fig. 3b), and the differences increased with particle size. Wilcoxon test using DFs for all of 1, 2, 4, and 8 μm particles (or 2, 4, and 8 μm particles by excluding 1 μm particles) showed moderate difference with $p = 0.052$ (or significant difference with $p < 0.05$) between the cluster 3 and cluster 4 subjects. In addition, Table 3 shows the biserial correlation coefficients of DF with cluster number for these cluster 3 and cluster 4 subjects, indicating association of DF with cluster number especially in the LLL for larger particles.

Local features

To evaluate the effect of airway constriction, average DD on the airway wall was presented in Figure 4 for the 4 μm diameter particles. C4 exhibited deposition hotspots (the red area in Fig. 4a) corresponding to the local branch constriction. Deposition was the largest at the first bifurcation distal to the left lower bronchus (LLB) constriction focused on the carina. Figure 4b–d presents the same location for HM, C2,

and C3 subjects, respectively. The DD hotspots were absent due to a lack of constriction at the LLB.

However, C2 had hotspots present at the bifurcations in the segmental and subsegmental region of LB10 corresponding to generations 4 and 5. Deposition in the child branches from the first bifurcation distal to the LLB accounted for 34.1% at 2 μm and 45.2% at 4 μm of total deposition in the LLL for C4. The same branches in C2 accounted for 9.7% and 5.9% of total deposition in the LLL at 2 and 4 μm, respectively. Figure 4a and b inserts show iso-surfaces of air speed at 2.5 and 5.0 m/s for the LLB location for C4 and HM subjects. The constriction induced a velocity increase at the center of the stream shown by the iso-surfaces, equating to higher inertia for particles to impinge on distal bifurcations. This was not present in the HM subject.

Discussion

We utilized imaging-based cluster membership in conjunction with subject-specific CFD lung models to assess the effects of cluster-specific imaging-based variables on air flow and particle deposition. The cluster-discriminant variables that may affect air flow and particle deposition were a structural variable D_h^* of the average normalized airway diameter in the LLL and a functional variable J of the lung deformation between TLC and FRC in the whole lung. The two variables were used to select 10 subjects for CFD and particle simulations (Table 2). We compared particle transport results between clusters through analysis of DF and DD and found that airway constriction has more discriminating effects on deposition statistics for larger particles ($>2 \mu$m).

While it is known that airway constriction in asthmatic lungs could lead to increased particle deposition,[36] the current study further supported the notion that cluster-specific airway structures could lead to different particle deposition patterns in severe asthmatics.

Intercluster and intracluster variability

To better understand intercluster and intracluster variability, the clustering procedure is briefly summarized as

TABLE 3. BISERIAL CORRELATION COEFFICIENTS OF LOBAR DEPOSITION FRACTIONS BETWEEN THE THREE CLUSTER 3 AND THREE CLUSTER 4 SUBJECTS WITH VARIOUS PARTICLE SIZES

Lobe	1 μm	2 μm	4 μm	8 μm
LUL	0.370	0.312	0.630	0.289
LLL	0.459	0.595	0.715	0.826
RUL	−0.041	0.018	0.298	0.407
RML	0.272	0.435	0.683	0.687
RLL	0.330	0.527	0.682	0.726
Whole lung	0.350	0.421	0.647	0.678

LLL, left lower lobe; LUL, left upper lobe; RLL, right lower lobe; RML, right middle lobe; RUL, right upper lobe.
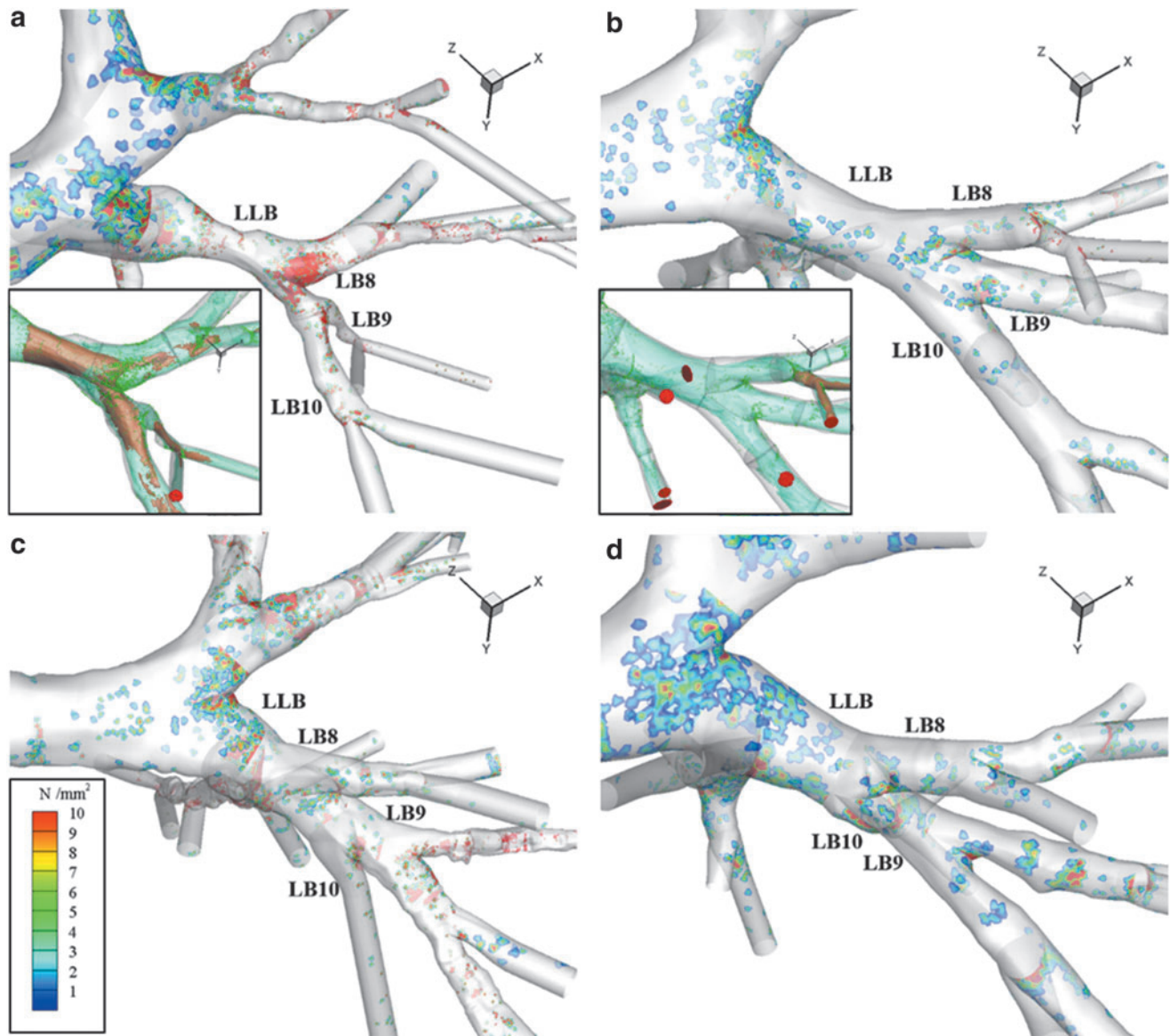
FIG. 4. Average DD plots of LLB for (a) C4, (b) HM, (c) C2, and (d) C3. DD presented as number of particles (N) per mm^2. Plots associated with 4 μm diameter particle simulations. HM and C4 subset figures show iso-surfaces of air speed at 2.5 m/s (green) and 5 m/s (brown) with final deposition locations at LLB and child branches. See Figure 1a for reference of the LLB location in the lung of these figures. DD, deposition density.

follows [Choi et al.[5] for details]. First, we conducted a principal component (PC) analysis for dimension reduction to identify major PCs that explain the majority of the variation in the standard scaled 57 imaging variables. The first PC (PC 1) was correlated with the parenchymal functions of J(Total) and ADI(Total) (anisotropic deformation index[5]), and the second PC (PC 2) was correlated with the segmental structures of WT*(sLLL) and D_h*(sLLL). We used the K-means method along with eight major PCs for clustering, resulting in stable cluster membership with large intercluster and small intracluster variations measured by three quantities of connectivity, Silhouette width, and Dunn index.[5]

We further used a nonparametric bootstrap analysis, based on resampling from the raw imaging data, to assess cluster stability measured by the mean of Jaccard similarity coefficients. Figure 5 showed the projection of the four color-coded cluster subjects and their respective cluster

means on two-dimensional PC 1 and PC 2 coordinates, demonstrating clear intercluster separation.

The most discriminant imaging-based variables listed in Table 1 were identified by a stepwise forward variable selection method, and the variations of these variables between clusters were assessed by Kruskal–Wallis statistical tests. The results indicated that these variables are significantly different among clusters (see the p-value in Table 1).

The intracluster variability of J(Total) and D_h*(sLLL) (Table 1 for the cluster means) was measured by the standard deviations of 0.33, 0.26, 0.22, and 0.17 for J(Total) and 0.038, 0.044, 0.044, and 0.046 for D_h*(sLLL) for clusters 1, 2, 3, and 4, respectively, as reported in Table II of Choi et al.[5] The locations of the 10 selected subjects were also marked in Figure 5, with each being distant from other cluster subjects. They exhibited statistically distinct cluster-specific features as illustrated by arrows ↑ (increase) and ↓
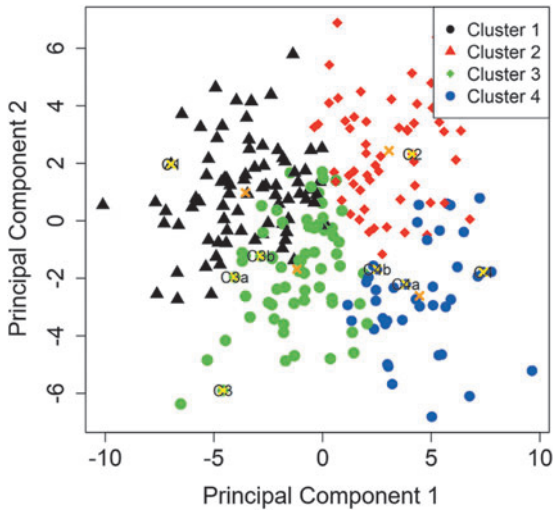
FIG. 5. Projection of the four color-coded cluster subjects and their respective cluster means (''x'') on PC 1 and PC 2 coordinates. PC, principal component.

(decrease) in Tables 1 and 2. Given the constraint of LES computational cost, this clustering-based sample extraction approach allows for reducing the number of CFD subjects while guaranteeing the selected subjects manifesting cluster-specific features.

While more CFD subjects are desirable for more reliable statistical analysis, this work confirmed that cluster-specific features affected particle deposition. Particularly, we focused on cluster 3 and cluster 4 subjects because they had the same asthma severity, but they were characterized by distinct airway structures. We performed biserial correlation analysis on the imaging-based and CFD-based variables of the selected three cluster 3 and three cluster 4 subjects.

The results showed the strong correlations of $r = -0.80$, -0.88, and 0.83 for D_h*(sLLL), J(Total), and DF in the LLL for 8 μm particles, respectively, between cluster 3 and cluster 4 subjects. A positive (or negative) correlation coefficient indicated an increase (or a decrease) of a variable in cluster 4. Thus, D_h*(sLLL) and J(Total) were inversely correlated with DF in the LLL. In contrast, the weak correlation of $r = -0.428$ and -0.386 for the peak inspiratory flow rate Q_{PI} and the $Re_{trachea}$ suggested that these flow-related variables were not significantly different between the two clusters although lung deformation measured by J(Total) was significantly different between them. Thus, an increase of DF in cluster 4 could be attributable to airway narrowing, particularly in the LLL.

Implications for drug delivery

One of the defining characteristics of severe asthma cluster 3 was central airway wall thickening without constriction. Thus, ICS particulates would be delivered preferentially to the lung periphery. If the goal is to treat central inflammation, an alternative formulation, with an increased particulate size, would likely provide improved central deposition in cluster 3 subjects. It is of note that 76% of patients grouped in cluster 3 used a high dosage of ICS and that cluster 3 was also associated with blood lymphopenia.[5]

Low DF in cluster 3 suggests that increasing ICS dosage with a small MMAD may not be effective for reducing inflammation at the segmental airways. This information may guide strategies using cluster-specific drug size to improve deposition targeting.

In addition, in cluster 2 and cluster 4 subjects, the observation that localized airway narrowing caused increased particle deposition in central airways provides insights for evaluating bronchodilator efficacy. Considering that asthma pathology is thought of as primarily a peripheral airway disease, local constrictions in central airways of subjects classified in cluster 2 and cluster 4 may prevent drug delivery to the peripheral airways and limit drug performance.

Comparison with existing literatures

Greenblatt et al.[37] conducted a positron emission tomography and CT imaging study of 12 bronchoconstricted asthmatic subjects (3 males and 9 females) and reported the correlation between the distribution of specific ventilation and the distribution of specific deposition ($r = 0.62$). These subjects were relatively young (about 20 years old) and had mild asthma with reversible obstruction by bronchodilator. They used an aerosol of ^{13}NH3-labeled isotonic saline delivered by a nebulizer, resulting in aerosol diameter ranging between 1.5 and 15 μm with a volume median diameter (VMD) of 4.9 μm. Methacholine bronchoconstriction challenge was performed before inhaling particles, mimicking an asthma attack. Thus, their study design is quite different from the current study in that the SARP subjects inhaled bronchodilator to improve breathing condition before imaging to acquire CT scans of good quality.

Fleming et al.[38] conducted a single-photon emission CT (SPECT) and CT imaging study of six male patients with moderate persistent asthma. They used Tc-99m-labeled albumin particles with VMD of 5.0 and 3.1 μm, respectively, for the large and small aerosol. They reported that regional aerosol deposition in the central conducting airways was greater in asthmatic subjects than control subjects.

There exist differences between the above two experimental studies and the current numerical study in terms of study design and imaging protocol. Nonetheless, for the sake of comparison we used the approach by Greenblatt et al.[37] to calculate the coefficient of variation among lobes (COV$_{Lobes}$) between QF and DF and then performed Pearson's correlation analysis for the 10 selected subjects.

The results showed strong correlation between lobar QF and DF for 1 μm ($r = 0.90$, $p = 3.5 \times 10^{-4}$) and 2 μm ($r = 0.70$, $p = 0.024$) particles. For 4 and 8 μm particles, however, no significant correlation was found ($p > 0.05$). Thus, our results agreed with Greenblatt et al.[37] and Fleming et al.[38] that QF, being equivalent to specific ventilation,[37] primarily governs regional particle transport and deposition for small particles; however, with increasing particle size local airway structure plays a more important role due to inertial effect, yielding greater central deposition (as seen in Figs. 2–4).

Limitations

Due to limited high-performance computing resources, we first selected one subject from each of the healthy male, healthy female, cluster 1, cluster 2, cluster 3, and cluster 4

cohorts, having a total of six subjects. To further investigate the effect of intracluster variability (namely, intersubject variability within clusters), we selected two additional subjects from each of cluster 3 and cluster 4 due to their potential clinical relevance that both were severe asthmatics but exhibited statistically different structural and functional features. More subjects are needed to get more reliable statistical analysis.

For imaging-based clustering,[5] we retrospectively analyzed image data from the SARP, where the study protocol did not include imaging of the mouth and throat. However, it is known that the geometry of upper airways, including the mouth, the oropharynx, and the larynx, is important in generating turbulent laryngeal jet on inspiration.[26,31] Miyawaki et al.[22] proposed a laryngeal model to generate a turbulent laryngeal jet in the trachea in case of lacking the upper airways. To reproduce homogeneous turbulent flow at the inlet proximal to the glottis, they used the SEM with the length scale and turbulent intensity determined by the $Re_{trachea}$. Their study showed that the deposition efficiencies predicted by the laryngeal model without the upper airways were in good agreement with those by the airway model, including the upper airways.

Nevertheless, the contribution of intersubject variability in the upper airways cannot be assessed due to lack of image data. It is worth noting that Fleming et al.[38] reported that the percentages of deposition in extrathoracic and thoracic airways were not significantly affected by disease. Furthermore, Miyawaki et al.[26] validated CFD-predicted particle deposition efficiency in the oral cavity with experimental data, showing that the efficiency depended on local Stokes number and Reynolds number. Thus, given the image data of oral cavity in the future, the total DF for the complete airway model could be assessed by the product of the oral deposition efficiency and the DF from the current study.

Another factor which might potentially affect DF is the particle release time. In this study, we used slow and deep breathing to model MDI activation[6] and released the particles at the start of inhalation. Most of the particles were deposited in less than 1 second. To assess the effect of the release time, we released the 1, 2, 4, and 8 μm particles at 0.3 seconds for the C4 subject and compared DFs with those released at the initial time. The results showed a slight increase of 3.5%–5.0%, which may be attributable to an increase in turbulent intensity experienced by the particles when released at a later time.

Our assessment is consistent with Longest et al.[6] that the changes in DFs were small, being less than 0.2% when comparing the initial release and continuous release during the first 0.2 and 0.5 seconds for the MDI. The %difference between their analysis and ours may be attributable to several factors. For example, since their airway model comprised a mouth–throat region with a DF of about 0.4, DFs in their segmental airways would be smaller compared with ours.

Summary

In conclusion, this study aimed to explore the notion of using imaging-based features to guide pharmaceutical drug treatment parameters, rather than broader metrics such as asthma severity. We demonstrated the effects of cluster-specific imaging-based features on particle deposition. A key message of the study is that airway narrowing, which characterizes only one of the two severe asthmatic clusters, induces greater particle deposition in the proximal airways and hence reduces the particle delivery into the small peripheral airways, which may be the primary target sites. The above effect was augmented for the large particles. The ability to differentiate severe asthmatics into subgroups by imaging-based features may help devise strategies for improved inhalational drug delivery.

Acknowledgments

Author Disclosure Statement

E.A.H. is a shareholder in VIDA diagnostics, a company that is commercializing lung image analysis software derived by the University of Iowa lung imaging group. He is also a member of the Siemens CT advisory board.

References

1. Byron PR: Drug delivery devices: Issues in drug development. Proc Am Thorac Soc. 2004;1:321–328.
2. Delvadia RR, Longest PW, and Byron PR: In vitro tests for aerosol deposition. I: Scaling a physical model of the upper airways to predict drug deposition variation in normal humans. J Aerosol Med Pulm Drug Deliv. 2012;25:32–40.
3. Delvadia RR, Wei X, Longest PW, Venitz J, and Byron PR: In vitro tests for aerosol deposition. IV: Simulating variations in human breath profiles for realistic DPI testing. J Aerosol Med Pulm Drug Deliv. 2016;29:196–206.
4. Cheng YS: Mechanisms of pharmaceutical aerosol deposition in the respiratory tract. AAPS Pharm Sci Tech. 2014; 15:630–640.
5. Choi S, Hoffman EA, Wenzel SE, Castro M, Fain S, Jarjour N, Schiebler ML, Chen K, Lin C-L, National Heart Lung, and Blood Institute's Severe Asthma Research Program: Quantitative computed tomographic imaging-based clustering differentiates asthmatic subgroups with distinctive clinical phenotypes. J Allergy Clin Immunol. 2017;140: 690–700.e698.
6. Longest P, Tian G, Walenga R, and Hindle M: Comparing MDI and DPI aerosol deposition using in vitro experiments and a new stochastic individual path (SIP) model of the conducting airways. Pharm Res. 2012;29:1670–1688.

7. Longest PW, Tian G, and Hindle M: Improving the lung delivery of nasally administered aerosols during noninvasive ventilation—An application of enhanced condensational growth (ECG). J Aerosol Med Pulm Drug Deliv. 2011;24:103–118.

8. Miyawaki S, Hoffman EA, and Lin C-L: Effect of static vs. dynamic imaging on particle transport in CT-based numerical models of human central airways. J Aerosol Sci. 2016;100:129–139.

9. Bos A, Van Holsbeke C, De Backer JW, Westreenen M, Janssens H, Vos WG, and Tiddens H: Patient-specific modeling of regional antibiotic concentration levels in airways of patients with cystic fibrosis: Are we dosing high enough? PLoS ONE 2015;10:e0118454.

10. Moore WC, Meyers DA, Wenzel SE, Teague WG, Li HS, Li XN, D'Agostino R, Castro M, Curran-Everett D, Fitzpatrick AM, Gaston B, Jarjour NN, Sorkness R, Calhoun WJ, Chung KF, Comhair SAA, Dweik RA, Israel E, Peters SP, Busse WW, Erzurum SC, Bleecker ER, and National Heart, Lung, and Blood Institute's Severe Asthma Research Program: Identification of asthma phenotypes using cluster analysis in the Severe Asthma Research Program. Am J Respir Crit Care Med. 2010;181:315–323.

11. Jarjour NN, Erzurum SC, Bleecker ER, Calhoun WJ, Castro M, Comhair SAA, Chung KF, Curran-Everett D, Dweik RA, Fain SB, Fitzpatrick AM, Gaston BM, Israel E, Hastie A, Hoffman EA, Holguin F, Levy BD, Meyers DA, Moore WC, Peters SP, Sorkness RL, Teague WG, Wenzel SE, and Busse WW: Severe asthma: Lessons learned from the National Heart, Lung, and Blood Institute Severe Asthma Research Program. Am J Respir Crit Care Med. 2012;185:356–362.

12. Moore WC, Bleecker ER, Curran-Everett D, Erzurum SC, Ameredes BT, Bacharier L, Calhoun WJ, Castro M, Chung KF, Clark MP, Dweik RA, Fitzpatrick AM, Gaston B, Hew M, Hussain I, Jarjour NN, Israel E, Levy BD, Murphy JR, Peters SP, Teague WG, Meyers DA, Busse WW, and Wenzel SE: Characterization of the severe asthma phenotype by the National Heart, Lung, and Blood Institute's Severe Asthma Research Program. J Allergy Clin Immunol. 2007;119:405–413.

13. Moore WC, Hastie AT, Li X, Li H, Busse WW, Jarjour NN, Wenzel SE, Peters SP, Meyers DA, and Bleecker ER: Sputum neutrophil counts are associated with more severe asthma phenotypes using cluster analysis. J Allergy Clin Immunol. 2014;133:1557–1563.e1555.

14. Fadl A, Wang J, Zhang Z, and Sung Cheng Y: Effects of MDI spray angle on aerosol penetration efficiency through an oral airway cast. J Aerosol Sci. 2007;38:853–864.

15. Longest P, and Hindle M: CFD simulations of enhanced condensational growth (ECG) applied to respiratory drug delivery with comparisons to in vitro data. J Aerosol Sci. 2010;41:805–820.

16. De Backer JW, Vos WG, Vinchurkar SC, Claes R, Drollmann A, Wulfrank D, Parizel PM, Germonpré P, and De Backer W: Validation of computational fluid dynamics in CT-based airway models with SPECT/CT. Radiology. 2010;257:854–862.

17. Lambert AR, O'Shaughnessy PT, Tawhai MH, Hoffman EA, and Lin C-L: Regional deposition of particles in an image-based airway model: Large-eddy simulation and left-right lung ventilation asymmetry. Aerosol Sci Tech. 2011;45:11–25.

18. Miyawaki S, Tawhai M, Hoffman E, Wenzel S, and Lin C-L: Automatic construction of subject-specific human airway geometry including trifurcations based on a CT-segmented airway skeleton and surface. Biomech Model Mechanobiol. 2017;16:583–596.

19. Yin Y, Choi J, Hoffman EA, Tawhai MH, and Lin C-L: A multiscale MDCT image-based breathing lung model with time-varying regional ventilation. J Comput Phys. 2013; 244:168–192.

20. Walenga RL, and Longest PW: Current inhalers deliver very small doses to the lower tracheobronchial airways: Assessment of healthy and constricted lungs. J Pharmaceut Sci. 2016;105:147–159.

21. Choi S, Hoffman EA, Wenzel SE, Castro M, Fain SB, Jarjour NN, Schiebler ML, Chen K, and Lin C-L: Quantitative assessment of multiscale structural and functional alterations in asthmatic populations. J Appl Physiol. 2015; 118:1286–1298.

22. Miyawaki S, Hoffman EA, and Lin C-L: Numerical simulations of aerosol delivery to the human lung with an idealized laryngeal model, image-based airway model, and automatic meshing algorithm. Comput Fluids. 2017;148: 1–9.

23. Tawhai M, Pullan A, and Hunter P: Generation of an anatomically based three-dimensional model of the conducting airways. Ann Biomed Eng. 2000;28:793–802.

24. Tawhai MH, Hunter P, Tschirren J, Reinhardt J, McLennan G, and Hoffman EA: CT-based geometry analysis and finite element models of the human and ovine bronchial tree. J Appl Physiol. 2004;97:2310–2321.

25. Choi S, Choi J, Miyawaki S, Hoffman E, and Lin C-L: Improved estimations of flow distribution using a 1-D resistance network model in asthmatic airways. Am J Respir Crit Care Med. 2016;193:A2495.

26. Miyawaki S, Tawhai M, Hoffman E, and Lin C-L: Effect of carrier gas properties on aerosol distribution in a CT-based human airway numerical model. Ann Biomed Eng. 2012; 40:1495–1507.

27. Haghighi B, Ellingwood ND, Yin Y, Hoffman EA, and Lin C-L: A GPU-based symmetric non-rigid image registration method in human lung. Med Biol Eng Comput. 2018;56: 355–371.

28. Yin Y, Choi J, Hoffman EA, Tawhai MH, and Lin C-L: Simulation of pulmonary air flow with a subject-specific boundary condition. J Biomech. 2010;43:2159–2163.

29. Choi S, Choi J, and Lin C-L: Contributions of kinetic energy and viscous dissipation to airway resistance in pulmonary inspiratory and expiratory airflows in successive symmetric airway models with various bifurcation angles. J Biomech Eng. 2018;140:011010.

30. Wongviriyawong C, Harris RS, Greenblatt E, Winkler T, and Venegas JG: Peripheral resistance: A link between global airflow obstruction and regional ventilation distribution. J Appl Physiol. 2013;114:504–514.

31. Choi J, Tawhai MH, Hoffman EA, and Lin C-L: On intra- and intersubject variabilities of airflow in the human lungs. Phys Fluids. 2009;21:101901.

32. Choi J, Xia G, Tawhai MH, Hoffman EA, and Lin C-L: Numerical study of high-frequency oscillatory air flow and convective mixing in a CT-based human airway model. Ann Biomed Eng. 2010;38:3550–3571.

33. Lin C-L, Tawhai MH, McLennan G, and Hoffman EA: Characteristics of the turbulent laryngeal jet and its effect

on airflow in the human intra-thoracic airways. Respir Physiol Neurobiol. 2007;157:295–309.

34. Lin C-L, Tawhai MH, McLennan G, and Hoffman EA: Computational fluid dynamics multiscale simulation of gas flow in subject-specific models of the human lung. IEEE Eng Med Biol. 2009;28:25–33.

35. Lin C-L, Lee H, Lee T, and Weber LJ: A level set characteristic Galerkin finite element method for free surface flows. Intl J Numer Meth Fluids. 2005;49:521–547.

36. Martonen T, Fleming J, Schroeter J, Conway J, and Hwang D: In silico modeling of asthma. Adv Drug Deliv Rev. 2003;55:829–849.

37. Greenblatt EE, Winkler T, Harris RS, Kelly VJ, Kone M, Katz I, Martin AR, Caillibotte G, and Venegas J: What causes uneven aerosol deposition in the bronchoconstricted lung? A quantitative imaging study. J Aerosol Med Pulm Drug Deliv. 2016;29:57–75.

38. Fleming J, Conway J, Majoral C, Katz I, Caillibotte G, Pichelin M, Montesantos S, and Bennett M: Controlled, parametric, individualized, 2-D and 3-D imaging mea- surements of aerosol deposition in the respiratory tract of asthmatic human subjects for model validation. J Aerosol Med Pulm Drug Deliv. 2015;28:432–451.

Address correspondence to:
Ching-Long Lin, PhD
Department of Mechanical Engineering
The University of Iowa
2406 Seamans Center for the Engineering
Arts and Sciences
Iowa City, IA 52242

E-mail: ching-long-lin@uiowa.edu